JOURNAL OF GEOPHYSICAL RESEARCH, VOL. 114, C12019, doi:10.1029/2009JC005363, 2009

Simulation of melt pond evolution on level ice

Eric D. Skyllingstad,[1] Clayton A. Paulson,[1] and Donald K. Perovich[2]

Received 6 March 2009; revised 31 July 2009; accepted 26 August 2009; published 18 December 2009.

[1] A melt pond model is presented that predicts pond size and depth changes, given an initial ice thickness field and representative surface fluxes. The model is based on the assumption that as sea ice melts, fresh water builds up in the ice pore space and eventually saturates the ice. Under these conditions, a water table is defined equal to the draft of the ice or sea level, and ponds are produced in ice surface depressions, much like lakes in a watershed. Pond evolution is forced by applying fluxes of heat at the pond surface and a radiative transfer model for solar radiation that penetrates the pond. Results from the model using forcing data from the Surface Heat Budget of the Arctic Ocean (SHEBA) experiment and representative pond parameters indicate that the model accurately simulates pond depth and fractional area over the summer melt season, with fractional area increasing linearly. Overall, ice albedo is affected primarily by the increase in pond coverage. Decrease in pond albedo from pond deepening has a much lower influence on the total albedo. Cases with predominately sunny conditions are shown to produce more rapid pond expansion than overcast cases. In both sunny and cloudy cases the fractional area increases linearly.

Citation: Skyllingstad, E. D., C. A. Paulson, and D. K. Perovich (2009), Simulation of melt pond evolution on level ice, *J. Geophys. Res.*, *114*, C12019, doi:10.1029/2009JC005363.

1. Introduction

[2] One of the strongest indicators of modern climate change is the decline in summer Arctic sea ice coverage that has occurred over the past 3 decades. During this time, summer sea ice extent has decreased from about 7.5×10^6 km^2 to roughly 5.7×10^6 km^2 in the late summer of 2006 [*Serreze et al.*, 2007]. Many factors control summer sea extent including warming from increasing greenhouse gases and natural variability of the atmospheric and ocean circulation. In general, climate prediction models indicate decreasing ice coverage, but at rates that are much less than the current observed behavior. *Stroeve et al.* [2007] examine this issue and suggest a number of reasons for model deficiencies. For example, they point out that anomalous atmospheric circulations associated with a persistent North Atlantic Mode pushed much of the older Arctic multiyear ice into the north Atlantic between 1989 and 1995. Remaining ice was thinner and more susceptible to summer melting. They also note that simplified ice parameterizations used in climate models may be underestimating the ice melting process. More recently, *Kay et al.* [2008] report on satellite observations showing a systematic decrease in cloud cover over the past decade. Their study, along with *Perovich et al.* [2008], indicates that increased solar radiation reaching the sea surface may explain the recent, record reduction in summer sea ice to levels below those predicted by climate prediction models.

[3] Melting of sea ice depends strongly on the albedo of the ice surface. For bare ice, typical albedo values vary from 0.5 to 0.7, with high values for frozen ice and low values corresponding to melting first year ice [*Hanesiak et al.*, 2001]. During summer, melt ponds form on the ice as snow and ice melt and act to lower the surface albedo as the ponds increase in depth and size. Albedo values for melt ponds are considerably less than bare ice, ranging from ~0.6 to ~0.15 depending on the depth of the ponds and pond bottom ice characteristics [*Perovich et al.*, 2002a]. This dependence of ice albedo on pond depth and areal coverage generates a positive feedback whereby the ice melting rate increases because of the greater absorbed radiation. Representing this process in a climate model is difficult because of the large variations in pond coverage that depend on the sea ice age, initial snow cover, ice permeability and the ice thickness variations. In this paper, we develop and test a melt pond model designed for level, undeformed ice. Our goal is to test a series of ice and pond assumptions and determine if a realistic pond model is possible given a set of basic ice/pond simplifications.

[4] Much of our limited understanding of pond coverage is based on observations of ponds using aircraft and field observations. From these data, statistical descriptions of ponds have been produced, for example, *Perovich et al.* [2002b] used aircraft observations to determine melt pond size distributions during the SHEBA summer melt season. Pond size and coverage are known to depend strongly on ice age and uniformity. Typically, smooth first year ice has large, shallow ponds with areal coverage up to 0.5, whereas

[1] College of Oceanic and Atmospheric Sciences, Oregon State University, Corvallis, Oregon, USA.
[2] Cold Regions Research and Engineering Laboratory, U.S. Army Engineer Research and Development Center, Hanover, New Hampshire, USA.

0148-0227/09/2009JC005363$09.00

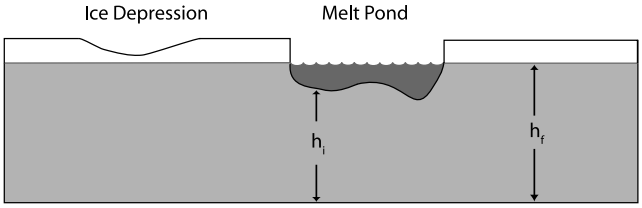

Figure 1. Schematic representation of a melt pond on ice with thickness, h_i, and ice draft of h_f. Pond depth is assumed equal to the difference between h_i and h_f.

multiyear ice develops relatively deep ponds with less areal coverage [*Fetterer and Untersteiner*, 1998; *Yackel et al.*, 2000]. Pond evolution is strongly controlled by the ice characteristics. In deformed, multiyear ice, ponds have been observed with maximum coverage in the early melt season, with gradual drainage and decreasing coverage over the summer. In contrast, ponds on first year or undeformed ice can increase in size and depth over the melt season, with coverage greater than 50% at the end of summer.

[5] Only a few attempts have been made to model the behavior of ponds on sea ice. *Taylor and Feltham* [2004] present a one-dimensional ice model where ponds are explicitly simulated using a thermodynamic and radiative model. Ponds are simulated as a separate phase in this model, however effects of pond areal coverage are not directly included. *Lüthje et al.* [2006] simulated areal pond coverage with a physically based method, where sea ice is treated much like a watershed system following arguments made by *Eicken et al.* [2004]. Basic equations for a water table are used with permeability set according to observed ice properties. Thermodynamic control of ponds is parameterized by enhancing the ice surface melting rate depending on the pond depth, thereby increasing melt rates to account for deep ponds having a lower albedo.

[6] Although both of the above models account for the relationship between pond depth and albedo, neither model addresses the combined effects of pond area coverage and depth on the overall ice albedo. Our goal in the present research was to develop a model that simulates the evolution of ponds driven by melting along the pond bottom and edges, as well as the effects of changing ice draft on pond depth. We take a simplified approach in dealing with the fresh water flux through the ice, basically assuming that meltwater elevation is independent of ice porosity and adjusts rapidly as ice thickness changes. Horizontal movement of meltwater is assumed to be instantaneous and the pond water depth is governed by the ice draft or sea level [*Perovich et al.*, 2003]. Radiative heating of the pond is calculated using a depth dependent, simplified radiation scheme described by *Skyllingstad and Paulson* [2007].

[7] Our model is designed for simulating pond evolution on relatively uniform ice similar to conditions observed during the summer melt period of SHEBA. We initialize the model using aerial images taken during SHEBA, and assume that pond depth is related to the pond albedo. Pond albedos depend on the thickness and the optical properties of the underlying ice [*Perovich et al.*, 2002a]. For pond bottoms with similar optical properties, darker ponds typically have thinner underlying ice and are deeper. Simulations are performed using observed fluxes over a 40 day period representing the primary melting season during the SHEBA experiment. The model is also tested using idealized conditions to examine the sensitivity of the simulated melt ponds to pond bottom and side heat exchange, and solar input.

[8] The paper is divided into 4 sections. In section 2, details of the pond model are presented along with a description of the initialization technique. Results from the model are presented in section 3 with comparisons between the pond depth evolution observed during SHEBA and simulated ponds. Experiments exploring the sensitivity of the pond model are also presented in this section. The paper concludes in section 4 with a summary and discussion.

2. Model and Initialization Description

2.1. Model Development

[9] Our approach to modeling pond behavior is based on the simple idea that melting sea ice is porous and allows for a relatively rapid movement of water to overcome buoyancy. With this assumption, fresh water in ponds is at a level equal to the local sea level defined by the ice draft as shown schematically in Figure 1. Ponds appear on the ice whenever the local ice surface is below the ice freeboard, defined as the difference between the ice thickness and the ice draft. We model ice and ponds using a two-dimensional grid with each grid cell having an ice thickness, h_i and water table height h_f. Ponds are defined as areas where the water table height is greater than the ice thickness, with pond depth defined as $d = h_f - h_i$. Gridded ice thickness can be initialized with topography derived either from direct observations (e.g., as in the work of *Lüthje et al.* [2006]), or by modeling the pond depth based on photographic images (described below). We also assume that the ice bottom is perfectly flat.

[10] Simulated pond growth results from bottom and sidewall melting, rather than through water flowing into the pond from surface melting. A number of assumptions are made to simplify the parameterization of pond melting. First, we assume that the pond water temperature is uniform within all ponds, which is partially justified by results from *Skyllingstad and Paulson* [2007] suggesting that even very light winds will thoroughly mix melt ponds. Pond water temperature is volume averaged every time step for all grid cells containing pond water. Averaging the pond water temperature across all ponds has the effect of increasing the growth of small ponds because of the depth dependence of solar radiation. Alternatively, we could calculate average pond temperatures for contiguous pond regions. However, we believe this approach would only have a minor effect on pond growth because the total absorbed heat is not directly affected by this simplification. Our next assumption is that the pond bottom for each grid cell is flat, allowing us to use the simplified bottom melt rate based on the area of the grid cell. Observed ponds, as shown in Figure 2, typically have a "U" shaped structure, with steep sidewalls and a uniform bottom, supporting this approach.

[11] Sidewall melting presents a more challenging problem in the grid box formulation. Because we only model a

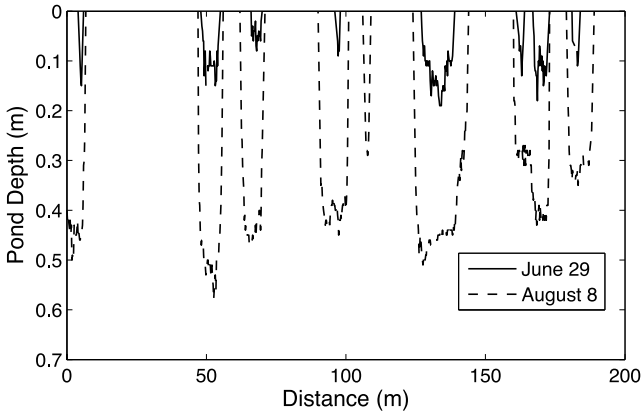

Figure 2. Pond depths from the SHEBA albedo line on 29 June 1998 and 8 August 1998.

single pond depth and ice thickness for each grid cell, we need to have a method for partial melting of ice along the pond edge to account for pond side melting. Our strategy is to label each grid cell that is on the edge of pond as a "border" cell containing both pond water and ice. For each border cell, we define a variable for the fractional water content, f_x, and determine which pond cells are adjacent to the border cell. Melting of the border cell is calculated by assuming that water from adjacent pond cells transfers heat to the pond edge, increasing f_x. When f_x equals or exceeds the grid width, Δx, the cell is converted to a pond cell. Border cell depth is set to the average depth of the adjacent pond cells.

[12] Pond water temperature for grid cells not adjacent to the pond edge is simulated by solving a one-dimensional heat budget:

$$\frac{dT}{dt} = \frac{Q_r + F_t - w_{ice}Q_L}{d} \tag{1}$$

where Q_r is the divergence of solar flux, F_t is the heat loss or gain through sensible, latent and long wave heat flux at the pond surface, w_{ice} is the ice melting velocity along the pond bottom defined below, and Q_L is the latent heat of fusion for ice [*Skyllingstad and Paulson*, 2007]. Ice melting rate, w_{ice}, is calculated using *McPhee et al.* [1987] as discussed below. A similar equation is used for border cells with the assumption that heat entering the fractional pond area in the border cell is distributed with neighbor pond cells along with heat loss from edge melting. For each border and neighbor cell, we compute a temperature change using

$$\frac{dT}{dt} = \frac{(Q_r + F_t - w_{ice}Q_L)f_x}{d(\Delta x + f_x)} - \frac{u_{ice}Q_L}{(\Delta x + f_x)} \tag{2}$$

where u_{ice} is the ice edge melting velocity. This equation accounts for the heat input through the fractional area in the first term, and the heat loss through melting along the pond edge in the second term.

[13] Solar flux, F_r, is parameterized using a radiative transfer equation developed using observations from fresh water capped leads taken between 17 June and 4 August during the SHEBA experiment [*Pegau*, 2002]. Radiative fluxes are calculated using

$$F_r(z)\downarrow = P_m F_{rn}\left(1 - e^{-K_m z}\right) \tag{3}$$

where P_m is the proportion of shortwave energy in the band m, F_{rn} is the net shortwave radiation at the sea surface, K_m is the diffuse extinction coefficient, and z is the depth below the surface. Information on the band characteristics is provided in Table 1. Fluxes defined using (3) include the effects of both direct and diffuse solar radiation; however, we do not attempt to account for radiation reflected from the sidewalls of ponds, which may effect the pond melting rates.

[14] Shortwave radiation reaching the pond bottom is either reflected upward by the ice under the pond or transmitted below the pond. Pond bottom albedo ranges from 0.7 to 0.2 depending on the thickness of the underlying ice and ice characteristics [*Podgorny and Grenfell*, 1996]. We modeled the bottom albedo as linearly decreasing from 0.5 to 0.3 in our basic 40 day simulations, and also present simulations that examine the sensitivity of the model to this parameter. Absorption of radiation reflected off the bottom is parameterized using (3) as if the depth were continuing to increase back to the surface:

$$F_r(z)\uparrow = P_m \alpha_b F_r(z_b)\left(1 - e^{-K_m[(z_b - z) + z_b]}\right) \tag{4}$$

where $F_r(z_b)$ is the radiation intensity at the bottom of the pond with depth z_b, and α_b is the pond bottom albedo. In (4), the depth dependence of wavelength properties in the formula are retained. Heating of the pond water is calculated as a function of pond depth by integrating the downwelling and upwelling radiation:

$$Q_r = \int_h F_r(z)\downarrow + \int_h F_r(z)\uparrow \tag{5}$$

Equations (4) and (5) can be used to estimate the effective pond albedo by calculating the total absorbed radiation and accounting for the radiation transmitted through the pond bottom:

$$(1 - \alpha_b)F_r(z_b) \tag{6}$$

[15] A plot of the predicted albedo integrated over the solar spectrum as a function of pond depth is presented in Figure 3 for three different pond bottom albedo values. For ponds with depths of ~0.4 m, albedo ranges from 0.1 to 0.4,

Table 1. Band Characteristics Used to Determine the Shortwave Radiation Absorbed in a Freshwater Layer[a]

Wavelength Range	P_m	K_m
350–700 nm (m = 1)	0.481	0.18
700–900 nm (m = 2)	0.194	3.25
900–1100 nm (m = 3)	0.123	27.5
>1100 nm (m = 4)	0.202	300

[a]P is a function of cloud conditions, and K is a function of material in the water.

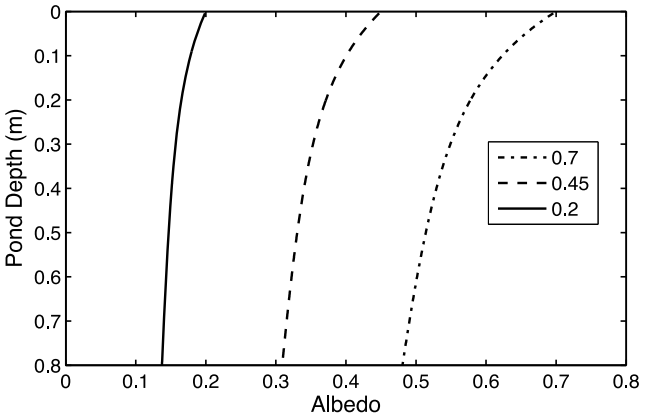

Figure 3. Pond albedo calculated as a function of pond depth for ponds with bottom albedo of 0.7, 0.45, and 0.2.

which is in agreement for first year pond albedo measured by *Hanesiak et al.* [2001] and for pond albedo measured by *Barber and Yackel* [1999]. Measured albedo values for shallow ponds (0.1 m) reported by *Fetterer and Untersteiner* [1998] ranged from 0.37 to 0.47 depending on the pond bottom albedo, also in general agreement with the modeled values shown in Figure 3.

[16] By using the one-dimensional empirical formula presented in (3) and (4), we ignore the effects of sunlight that enters the pond at an angle and interacts with the pond sidewall. For small ponds, this could be significant, but will in general be much smaller than the integrated sunlight defined by the pond surface area. We also assume that the pond radiative properties, cloud conditions and overall weather are similar to those of the fresh water capped lead that was used to formulate (3) and (4).

[17] Surface fluxes of longwave radiation along with sensible and latent heating, F_t, are prescribed at the pond surface. For the simulations presented here, F_t is calculated using bulk formula for sensible and latent heat, along with measured downward longwave radiative fluxes and estimated upward infrared flux, using data collected during the SHEBA experiment. Methods for calculating fluxes are presented below in the results section.

[18] Melting along the pond bottom and sidewalls is parameterized using transfer coefficients developed by *McPhee et al.* [1987] that account for the differing diffusivities of salt and heat. Ice melting rate is calculated using

$$\langle u_i T_o \rangle = w_{ice} Q_L \tag{7}$$

$$\langle u_i S_o \rangle = w_{ice}(S_w - S_i) \tag{8}$$

where S_w is the pond salinity at the ice edge, S_i is the ice salinity, $w_{ice} = \rho_i/\rho_o m_i$ represents a velocity of the ice surface associated with ice growth or melting, ρ_o is the density of the pond water, $\langle u_i T_o \rangle$ and $\langle u_i S_o \rangle$ represent the subgrid heat and salinity boundary fluxes into the pond near the ice edge, respectively, m_i is the ice melting or growth rate, ρ_i = 920 kg m^{-3} is the ice density, and $Q_L = L/c_p$, where $L = 3.34 \times 10^5$ J Kg^{-1} is the latent heat of fusion and c_p = 4000 J (Kg °C)$^{-1}$ is the specific heat of water. Scaling (7) and (8) with friction velocity u_* and integrating vertically results in two nondimensional functions

$$\Phi_T = \frac{T(x_i) - T_w}{(w_{ice} Q_L)/u_*} \tag{9}$$

$$\Phi_S = \frac{S(x_i) - S_w}{w_{ice}(S_w - S_i)/u_*} \tag{10}$$

where $T(x_i)$ and $S(x_i)$ are the temperature and salinity at the nearest grid point to the pond bottom or edge.

[19] Equations (9) and (10) can be combined and simplified by replacing the wall temperature with the freezing temperature at S_w, or $T_w = -mS_w$, where $m = -0.054$ yielding

$$mS_w^2 + \left[T(x_i) - mS_i + \frac{\Phi_T Q_L}{\Phi_S}\right] S_w - \left[T(x_i) S_i + \frac{\Phi_T Q_L}{\Phi_S} S(x_i)\right] = 0 \tag{11}$$

Ice melting rate, w_{ice}, is calculated by solving (10) with exchange functions defined as

$$\Phi_{T,S} = \Phi_{turb} + 1.57 \left(\frac{u_* z_o}{\nu}\right)^{\frac{1}{2}} \left(\frac{\nu}{\kappa_{T,S}}\right)^{\frac{2}{3}}$$
$$\Phi_{turb} = 2.5 \ln\left(\frac{z}{z_o}\right) \tag{12}$$

where z_o = 0.002 m, $\nu = 1.4 \times 10^{-6}$ m^2 s^{-1} is the molecular viscosity, and $\kappa_T = 1.4 \times 10^{-7}$ m^2 s^{-1} and $\kappa_S = 7.4 \times 10^{-10}$ m^2 s^{-1} are the molecular diffusivities for heat and salinity, respectively. For most ponds, the salinity is low (<4 psu) [*Eicken et al.*, 2002], consequently the salinity of the pond water does not have a large influence on the edge and bottom melting rates. Simulation of pond temperature is simplified by assuming that heat is instantly redistributed in ponds by wind forcing and buoyant convection, leading to a uniform pond temperature. As mentioned above, we accomplish this redistribution by computing an average pond water temperature for all grid locations containing pond water.

[20] A key parameter in the melting rate parameterization is the friction velocity, which is used to scale the exchange rates in (9)–(10). In the work of *Skyllingstad and Paulson* [2007], friction velocities were found to vary from pond sidewalls to pond bottom, with values ranging from 0.0005 m s^{-1} to 0.001 m s^{-1}. These were calculated for ponds having very weak wind forcing and basically smooth sides. Direct estimates of u_* ranging from 0.009 to 0.012 from beneath sea ice have been reported by *McPhee* [1992] for currents between 0.09 and 0.17 m s^{-1}. Here, to select representative pond sidewall and bottom friction velocities (v_* and u_*, respectively) we performed a sensitivity analysis over a range of v_* and u_*. Results from this analysis, presented in more detail in the results section, provide a range of pond depth and fractional area values similar to observed ponds during SHEBA. Based on the sensitivity results, we chose values of v_* = 0.014 and u_* = 0.005 m s^{-1} for the "best guess" control experiment presented below.

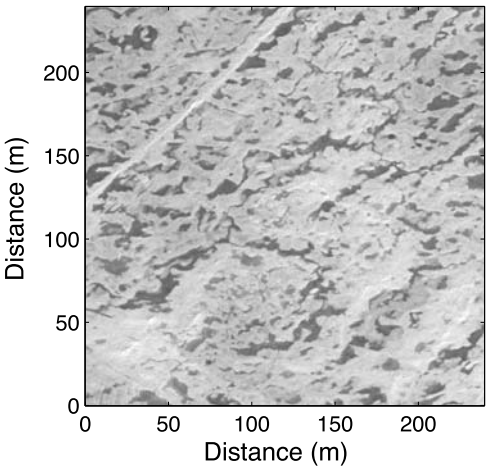

Figure 4. Gray scale image converted from a color areal photograph taken on 30 June 1998 during the SHEBA experiment. Resolution of this image is ~0.6 m.

2.2. Pond Initialization

[21] Area observations of ponds are typically limited to aircraft surveys with limited information regarding pond depth or significant ice characteristics such as thickness and surface topography. Direct pond observations [e.g., *Barber and Yackel*, 1999; *Fetterer and Untersteiner*, 1998; *Perovich et al.*, 2003] provide a snapshot of pond depth and ice thickness, but are lacking in a true field description of pond features. In the modeling study of *Lüthje et al.* [2006], 2.5 m resolution ice topography estimated from aerial laser altimetry data [*Hvidegaard and Forsberg*, 2002] were used as initial data for modeling ponds. However, they did not have a direct set of pond measurements to verify their results.

[22] Here we apply an indirect method for estimating an initial pond state given aerial photographs of observed ponds. Our method is similar to a technique developed by *Sneed and Hamilton* [2007] for estimating pond depths on the Greenland Ice Sheet. In our method, we rely on the relationship between pond albedo and pond depth, and on direct measurements of pond depths taken during the SHEBA experiment, whereas *Sneed and Hamilton* [2007] use the radiative transfer based on the spectral properties of pure water.

[23] Pond albedo can be calculated from (3) and (4) by comparing the input radiation with the total flux that is absorbed in the pond or transmitted through the pond bottom. Examples of albedo as a function of pond depth are shown in Figure 3 for range of α_b values between 0.7 and 0.2. Using aerial photographs converted to gray scale, we can estimate pond albedo, α_p, by computing the ratio of the gray scale of ponds with the gray scale of ice

$$\frac{\alpha_p}{\alpha_i} = \frac{B_p}{B_i} \tag{13}$$

where ice albedo, α_i = ~0.6, for bare summer ice [*Perovich et al.*, 2002a; *Hanesiak et al.*, 2001] and B_p and B_i represent image brightness of ponds and ice, respectively.

[24] Solving for α_p requires an estimate of the ice brightness intensity, which can be determined by examining the histogram of brightness values for a gray scale image. We apply this method to an early melt season photograph taken during the SHEBA experiment (Figure 4) having resolution of 0.6 m. Brightness values for this image define a bimodal distribution, as shown in Figure 5, which has a near-normal appearance centered around brightness value 150, with an extended tail over the low end of brightness intensity. The tail of brightness values represent ponds, suggesting a value of B_i = ~130 as a cutoff for pond water versus ice.

[25] Calculation of the pond depth from the estimated pond albedo requires a value for the pond bottom albedo. As Figure 3 shows, changes in the pond bottom albedo have a significant impact on the relationship between pond depth and pond albedo. Pond albedo is a better indication of pond depth when the pond bottom albedo is high. Because our goal in this study is to build a realistic pond initial condition, we treat the pond bottom albedo as an adjustable parameter and select a value of α_b = 0.5 through trial and error. Are strategy basically calibrates the pond albedo to depth for the SHEBA conditions, and is not necessarily applicable to other aerial photograph surveys of melt ponds. Using (3)–(4), we generated a look up table of pond depth as a function of albedo and transform estimated albedo calculated with (13) to pond depths as presented in Figure 6. Pond depths in the plot are for the most part between 0.1 and 0.2 m, with a few ponds having deeper regions near 0.5 m. Unfortunately, we do not have an areal image that covers the SHEBA albedo line presented in Figure 2 near the beginning of the melt season. Nevertheless, since the 30 June image was taken very near the location of the albedo line, we believe the pond depth map shown in Figure 6 is a reasonable estimate of the actual conditions.

[26] The inversion method provides an estimate for pond depths, but we still need to know the variations in the ice thickness for ice surrounding the ponds. Here we assume that the surrounding ice is flat and has a prescribed ice draft (2.5 m in the control case). Initial ice thickness can then by

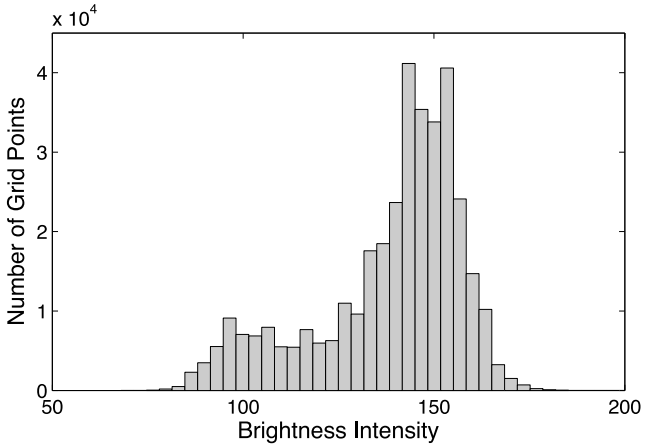

Figure 5. Distribution of brightness intensity for the image shown in Figure 4. Values above ~130 are considered ice surface, whereas the relatively flat distribution between 90 and 130 is indicative of ponds.

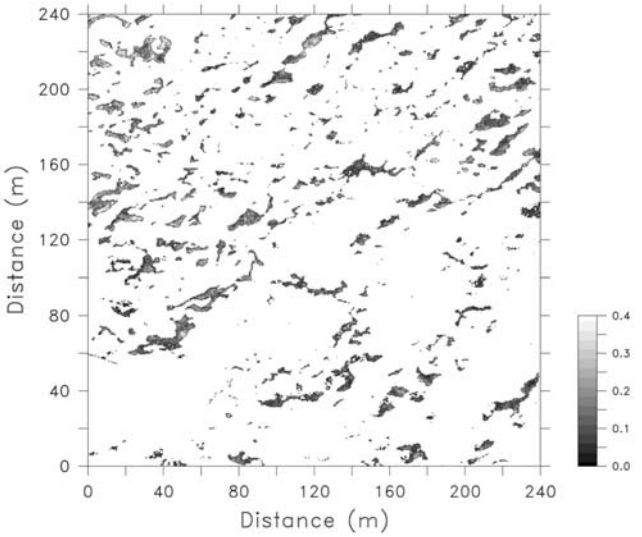

Figure 6. Pond depth (m) diagnosed from an aerial photograph (shown in Figure 4), using the relationship between pond albedo and pond depth described in the text.

estimated using the diagnosed pond depths (d) along with the relationship between h_f and h_i, where

$$h_f = \frac{\rho_{ice}}{\rho_{water}}\left[\frac{n_p\overline{h}_p + n_i\overline{h}_i}{n}\right]$$
$$\overline{d} = h_f - \overline{h}_p \tag{14}$$

where $\overline{h}_p = \frac{1}{n_p}\sum_{n_p} h_i$ is the average ice thickness under ponds, $\overline{h}_i = \frac{1}{n_i}\sum_{n_i} h_i$ is the average ice thickness for ice without ponds, $\overline{d} = \frac{1}{n_p}\sum_{n_p} d_i$ is the average pond depth from the aerial photography analysis, and $n_i + n_p = n$ is the total number of points. Equation (14) is solved for $\overline{h}_i$ which is assumed to have a constant value

$$\overline{h}_i = \frac{n\frac{\rho_{water}}{\rho_{ice}}h_f - n_p\left(h_f - \overline{d}\right)}{n_i} \tag{15}$$

and ice thickness for pond points is calculated using $h_p(x, y) = \overline{h}_i - d(x, y)$.

[27] One significant issue with the pond initialization method concerns the assumption of a flat ice surface. In reality, the ice surface in the region around ponds is likely to be somewhat lower than the average, which will lead to ponds expanding as the overall ice melts and the water table moves above the ice surface. By assuming a flat ice surface, pond expansion can only occur through sidewall melting. As a partial compensation for this simplification, we do not account for melting of the ice edge above the pond, but assume that the sidewall melting leads directly to pond expansion.

3. Results

3.1. Control Simulation

[28] A series of experiments are presented beginning with a control simulation representing forcing conditions from the SHEBA melt season. As stated in the introduction, we assume that the ice is porous throughout the experiments, with pond levels equaling the local sea level. In the SHEBA experiment, ponds began forming around mid-June as surface snow melted. Pond fractional coverage for the albedo line increased to about 28% and then decreased in the latter half of June as the ice became permeable. Pond drainage continued until late June when the pond fraction reached ~12–15% on 26 June. Thereafter, pond coverage on the albedo line increased gradually to a maximum of ~38% in early August. Pond coverage in the region around the SHEBA camp estimated from aerial photographs ranged from ~14% at the end of June to ~23% in the beginning of August [*Perovich et al.*, 2002a]. We assume that the late June minimum in pond fractional area represents the time when pond levels reached equilibrium with the local sea level, hence our choice of the 30 June image for initializing the model.

[29] Model forcing for the SHEBA control case is based on observations of the temperature and specific humidity taken between 27 June 1998 and 6 August 1998 representing the time period between the beginning of pond drainage and the maximum pond coverage in August. Direct observations of heat and moisture flux from ponds, for example by eddy covariance methods, were not made during the SHEBA field program. As a substitute, we employ flux estimates based on simple bulk formula for sensible and latent heat [see *Stull*, 1988, p. 262]

$$F_{sh} = -\rho_a C_p C_H U\left(T_r - T_p\right)$$
$$F_{lh} = \rho_a L_v C_H U(q_s - q_r) \tag{16}$$

where $\rho_a = 1.29$ kg m^{-3} is the air density, $C_p = 4000$ J K^{-1} kg^{-1} is the air heat capacity, $C_H = 1.5 \times 10^{-3}$ is the transfer coefficient for heat and moisture, U is the wind speed, T_r is the measured atmospheric reference temperature from 2.5 m height, T_p is the pond temperature, $L_v = 2.5 \times 10^6$ J kg^{-1} is the latent heat of vaporization for water, q_s is the saturation specific humidity and q_r is the measured specific humidity from 2.5 m height. Although more sophisticated methods for estimating C_H are available, tests of the pond model suggest that results are relatively insensitive to this parameter. Downwelling longwave fluxes were measured during SHEBA. We estimate upwelling longwave flux using

$$F_{lw}\uparrow = \varepsilon\sigma T_p^4 \tag{17}$$

where the emissivity, $\varepsilon = 0.97$, and $\sigma = 5.67 \times 10^{-8}$ W m^{-2} K^{-4} is the Stefan-Boltzmann constant.

[30] Plots of the radiative and surface heat flux terms using (16) and (17) are shown in Figure 7. Short wave fluxes during the 40 day period ranged from daily high values of about 500 W m^{-2} to evening minimum values of ~50 W m^{-2}. Net long wave flux was typically a function of cloud cover, with clear conditions generating surface cooling of 50–60 W m^{-2}. Cloud cover often produced a downward flux with surface warming between 10 and 20 W m^{-2}. Both sensible and latent heat varied over the time of record with magnitudes frequently less than 10 W m^{-2},

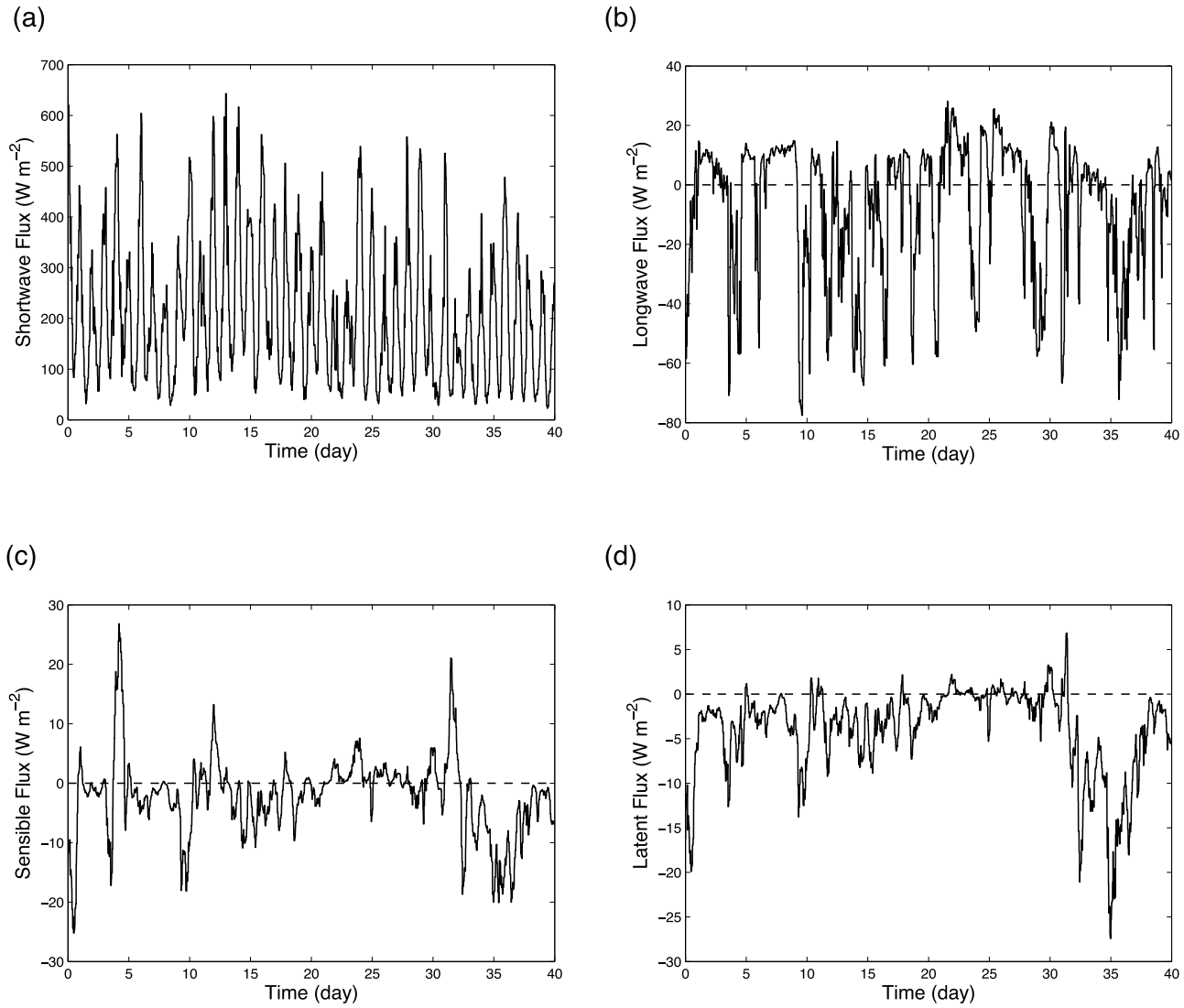

Figure 7. Flux of (a) shortwave radiation, (b) longwave radiation, (c) sensible heat flux, and (d) latent heat flux for the SHEBA experiment for the 40 day period starting on 27 June 1998 (day 178). Integrated solar flux is 210 W m^{-2}; combined longwave, sensible, and latent fluxes yield an integrated value of -8.2 W m^{-2}.

except in late July/early August when conditions began cooling with the onset of autumn.

[31] Background ice melting rates for the control experiment were set according to SHEBA ice mass measurements, which indicated surface melting rates of $\sim$1.5 cm d^{-1} and ice bottom melting rates of $\sim$0.5 cm d^{-1} between late June and early August [*Perovich et al.*, 2003]. Ice surface melting is only performed in regions not covered by a pond, whereas the bottom melting is uniformly applied.

[32] Two key parameters needed to simulate the pond heat flux and melting rates accurately are the pond bottom and sidewall friction velocities, u_* and v_*, respectively. Measurement of these parameters in actual ponds has not been conducted and only limited, idealized large eddy simulation results exist for estimating pond friction velocities [see *Skyllingstad and Paulson*, 2007]. In the absence of measurements, we treat u_* and v_* as adjustable parameters and perform a series of pond sensitivity experiments to determine values for friction velocity that yield pond fractional area and pond depths similar to observations from the SHEBA albedo line presented in Figure 2. Figure 8 shows contour plots of pond fractional area and pond depth for a range of u_* and v_* between 0.001 and 0.016, calculated for increments of 0.001, and using the 40 day forcing described above. In general, results show that increasing friction velocity leads to increased pond bottom or wall flux. Variations between u_* and v_* lead to counteracting changes in the pond depth and fractional area; large fractional area coincides with shallow ponds, whereas small fractional area corresponds with deep ponds. For our control case, we selected values of u_* and v_* (0.005 m s^{-1} and 0.014 m s^{-1}, respectively) that yield a pond fractional area similar to observations from SHEBA aircraft surveys and pond depths consistent with the SHEBA albedo line shown in Figure 2. As shown by Figure 8, our selection is somewhat arbitrary given that a range of u_* and v_* will yield similar fractional area and pond depth.

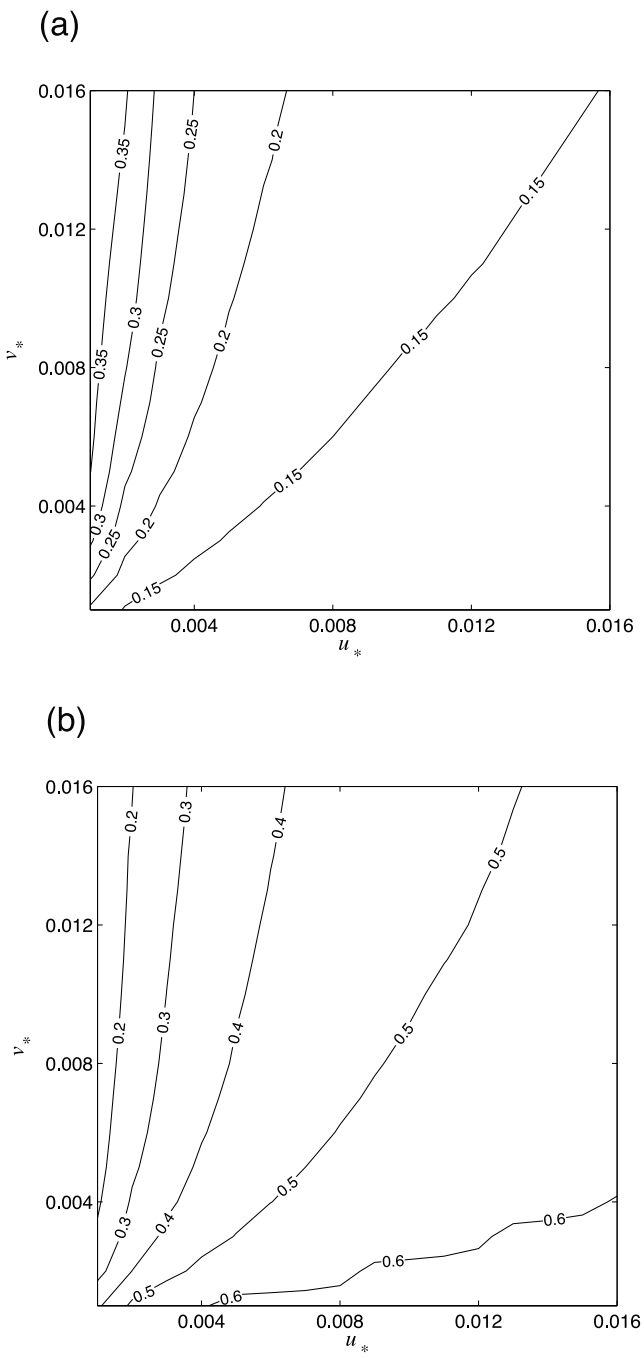

Figure 8. Contours of (a) pond fraction and (b) pond depth as a function of pond bottom friction velocity, u_*, and pond sidewall friction velocity, v_*, after 40 days. Forcing is the standard SHEBA control case.

[33] Pond depth for the control simulation at 40 days is shown in Figure 9 for comparison to the initial state shown in Figure 6. Overall, pond depths and sizes increase in the simulation with typical initial pond depths of ~0.15–0.2 m increasing to ~0.4–0.6 m. Many of the ponds merge to form large, complex features by the end of the simulation, agreeing with aerial observations [*Perovich et al.*, 2002b]. We do not produce new ponds in the simulation because of the imposed, flat ice surface, which is in contrast to observations that show small pond formation from bare ice. Consequently, simulated ice fractional area is likely to underestimate actual conditions.

[34] A sample cross section from the model at x = 200 m (Figure 10) shows the pond characteristics at three different times in the simulation. Comparison of this plot with Figure 2 provides a measure of the ability of the model to simulate pond attributes assuming pond water clarity equivalent to fresh water capped leads. Many of the modeled ponds show deepening from about 0.1 m to 0.4 m over the ~40 day time period, in comparison to observed depths of about 0.45 m over the same time period. Lateral growth of the simulated ponds also appears to underestimate observed pond behavior with the model tending to maintain pond widths similar to the initial state. As mentioned above, this aspect of the simulation is produced by the flat ice surface assumption. Actual ponds grow from both sidewall melting and flooding of surrounding low ice surfaces, due to decreasing ice thickness and ice draft. Deeper ponds are evident in the modeled case, but these are for ponds that are initialized with a greater depth than the observed cases. Both observed and modeled ponds that begin in close proximity tend to merge and form larger ponds, for example as shown by the pond between 60 and 70 m in the model, and near 175 m in the observations.

[35] Average simulated pond temperature (not shown) ranges from ~0.6°C at the beginning of the simulation to ~0.35°C after 40 days, decreasing as the solar forcing is reduced. These temperatures are in the same range as observed values (T. Grenfell, personal communication, 2006) and results from large eddy simulation of ponds [*Skyllingstad and Paulson*, 2007].

[36] Plots of the horizontally averaged pond fractional area, depth, albedo, and total ice surface albedo (assuming a bare ice albedo of 0.6) are shown in Figure 11 for the control simulation with constant pond bottom albedo of 0.5 and with variable pond bottom albedo decreasing linearly from 0.5 to 0.3 over the 40 day simulation. The variable pond bottom albedo is based on the observation that ice

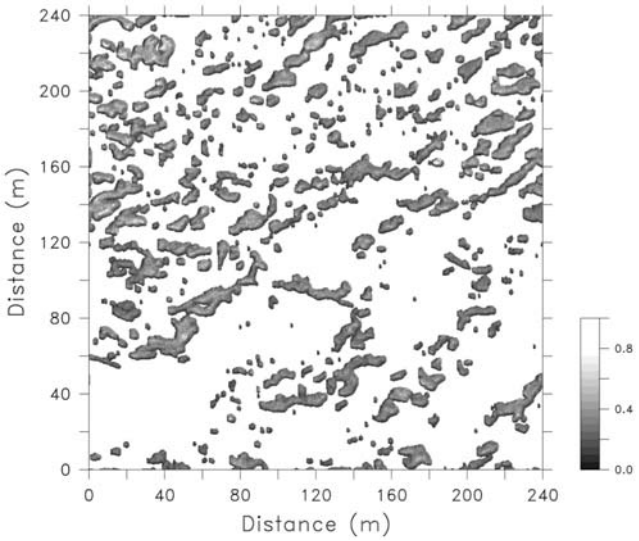

Figure 9. Pond depth (m) predicted by the model after 40 days of forcing in the control experiment.

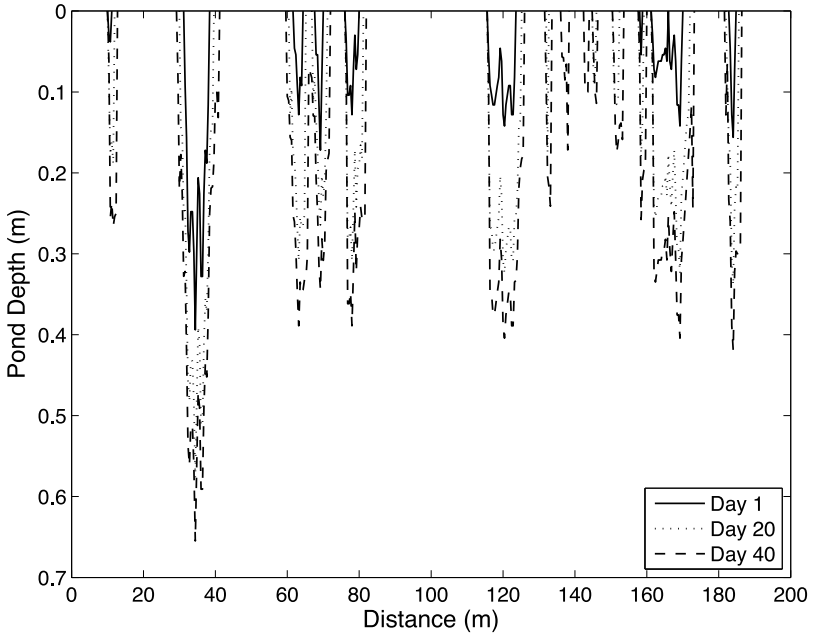

Figure 10. Simulated pond depths from x = 200 m in the control case with constant bottom albedo.

under ponds generally darkens because air bubbles escape from the ice, and the ice often thins more rapidly under ponds because of more rapid bottom melting. Overall, pond fraction increases at a nearly constant rate from an initial minimum of 0.1 to a final value of 0.28. Pond fraction is nearly the same in both the constant and variable bottom albedo cases, suggesting that pond bottom albedo is secondary in determining the melting rate of sea ice by pond water. Average pond depth is initially about 0.12 m and increases to a stable value of about 0.28 m at 30 days. As with the fractional area, pond bottom albedo has only a small influence on the pond depth. Additional heat from reflected solar radiation off the pond bottom in the constant albedo case produces a slight increase in pond fraction and depth.

[37] In the constant bottom albedo case, pond albedo gradually decreases from 0.29 to a near constant value of 0.24 on about day 30, representing a total change of about 0.05. Pond albedo in the variable case basically follows the linear decrease forced by the assigned variable bottom albedo combined with the depth dependent albedo change, yielding a final pond albedo of ~0.15, and a total pond albedo change of ~0.14. Although pond bottom albedo is not critical for pond growth, it is important to note that solar radiation that penetrates pond bottoms (low albedo) is absorbed in the underlying ice and ocean boundary layer. Ultimately this heat can go toward increasing the ice bottom melting rates.

[38] Albedo of the total ice surface is a function of both the individual pond albedo and the pond areal coverage. As pond fraction increases, the total albedo decreases. Consequently, plots of the average total albedo (Figure 11c) show a more pronounced influence of the pond lateral growth in comparison to the depth-dependent pond albedo. For example, in the constant bottom albedo case, the total albedo decreases from 0.57 to almost 0.5 for a total change of about 0.07. This compares with an average pond albedo change of 0.05, indicating the important role that pond coverage has in setting the ice surface albedo. Results from the variable bottom albedo case indicate a total albedo decrease of ~0.1, which is less than the change in the average pond albedo. The effects of decreasing pond albedo in this case are reduced because of the averaging with ice albedo of 0.6.

[39] These results indicate that the effects of pond depth on pond albedo are not always the main aspect of ponds that affect the ice surface albedo. While the pond albedo reaches a steady value around day 30 in the constant bottom albedo case, total albedo continues to decrease because of the lateral melting of ponds and increased pond area. Consequently, the expansion of ponds is a key factor in the decrease of total ice surface albedo.

[40] Comparison of our results with observations from *Perovich et al.* [2002a] suggest that the pond model underestimates pond and total ice albedo for the variable pond bottom albedo case. For example, observed pond albedo for "dark" ponds in the SHEBA albedo line decreased from ~0.4 to ~0.1 during the July time period. Total albedo observed from aircraft indicated a decrease from ~0.55 to ~0.44 [*Perovich et al.*, 2002b], however these estimates include the substantial increase in lead coverage in the beginning of August. Pond fraction estimates varied significantly in the observations with the albedo line showing an increase from about 15% to 38%, whereas aerial estimates suggest an increase from about 15% in late June to 24% in early August, which is more in line with the pond model results. In our simulations, the initial ice fraction is slightly lower because of the image selected for the initial condition. However, we predict an increase in coverage of about 19%, which falls between the observed albedo line increase and aircraft estimates. Overall, the linear behavior of pond coverage and total albedo predicted by the model is consistent with observed trends over the main summer melting season. Likewise, the more rapid decrease in pond albedo at

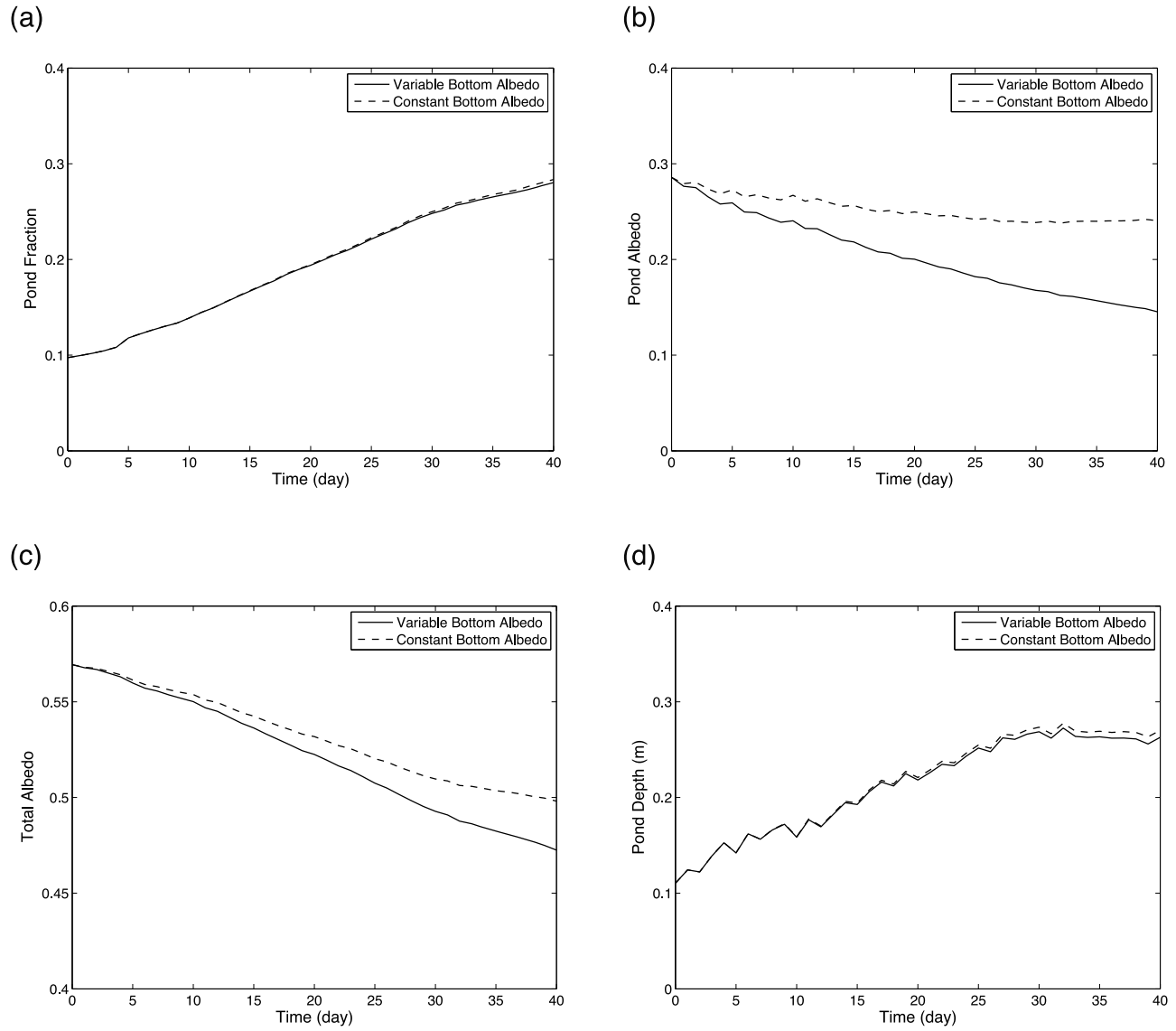

Figure 11. Control simulation average (a) pond fraction, (b) pond albedo, (c) total albedo (assuming ice albedo of 0.6), and (d) pond depth (m) for variable pond bottom albedo (solid) and constant pond bottom albedo (dashed).

the beginning of the simulation is similar to observed albedo from the albedo line showing a steep decline in pond albedo in late June followed by an almost constant minimum value later in July [*Perovich et al.*, 2002a, Figure 5].

[41] We note that our results do not agree with photographic-based observations of ponds on deformed multiyear ice presented by *Fetterer and Untersteiner* [1998]. Pond levels in deformed, thick ice often have a level above sea level (which is assumed to be the pond level in our model), and therefore can lose water through drainage via percolation or channels. Consequently, the pond schematic presented by *Fetterer and Untersteiner* [1998] shows decreasing pond size as the summer progresses, in reverse of the behavior modeled here.

[42] In addition to the ice surface assumptions used in the model, it is important to note that the radiative transfer coefficients used in (3)–(4) may not be representative for melt ponds. These coefficients are derived from measurements taken in a lead capped by nearly fresh water (salinity of about 2 psu), which did not have significant impurities. Melt ponds, however, can contain sediment and atmospheric aerosols, which accumulate on the ice below the pond. Both of these contaminants will change the effective transmittance of the pond water and could affect absorbed solar radiation both within the pond water and along the pond bottom and perimeter. At this time, we are not aware of measurements to support parameterizing this effect.

3.2. Sensitivity Experiments

3.2.1. Cloud Cover

[43] Variations in cloud cover are known to affect the heat budget of the Arctic and are thought to influence the decreasing observed summer ice pack coverage [*Kay et al.*, 2008]. Clouds have two main impacts on the surface radiative budget; they block solar radiation and reduce surface heating, and they absorb and emit infrared radiation,

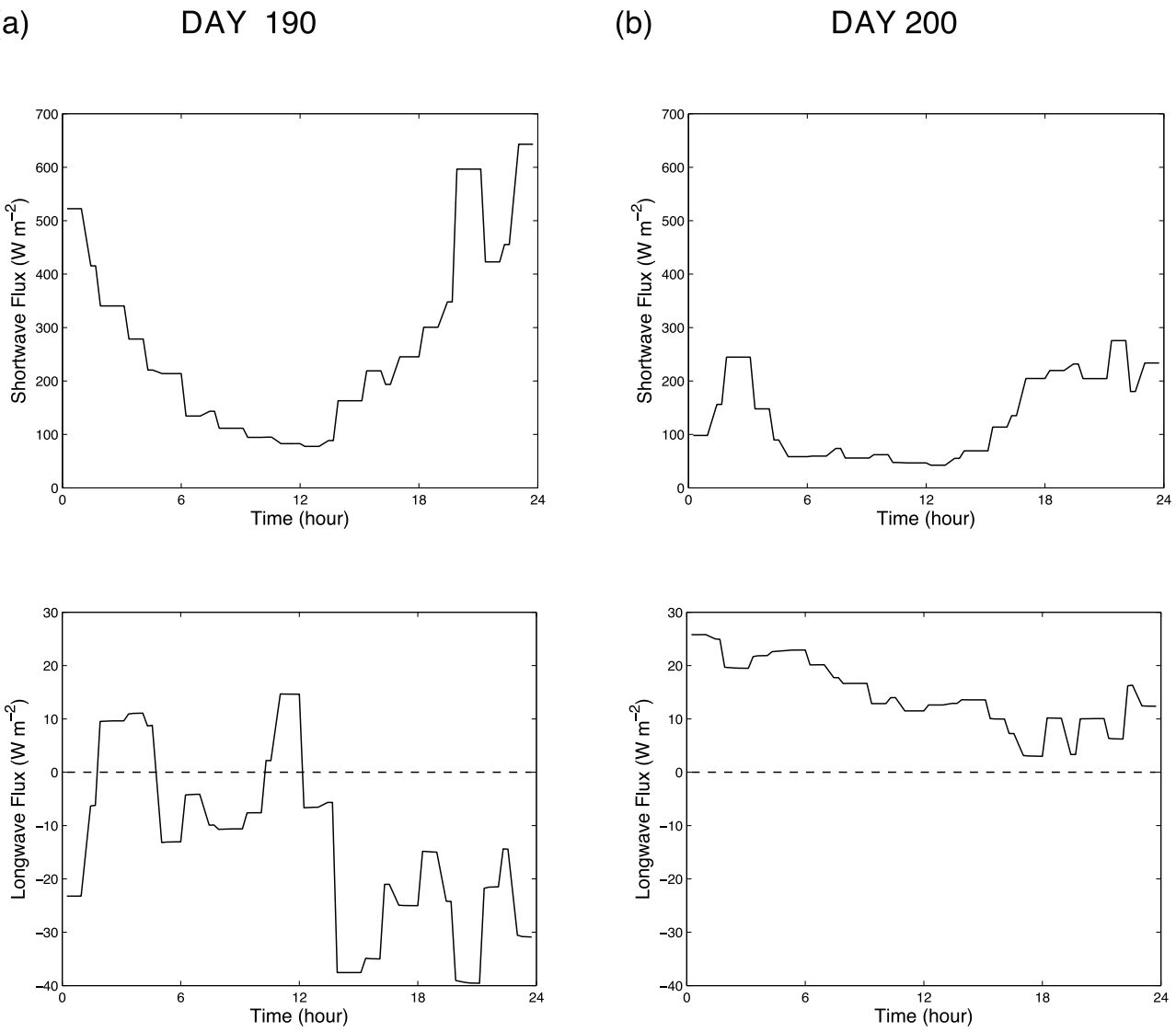

Figure 12. Fluxes of (top) shortwave and (bottom) longwave for (a) day 190 and (b) day 200, representing ''sunny'' and ''cloud'' days, respectively. The 24 h time series for each day starts at 12 noon.

limiting cooling of the surface through radiative heat loss. Both of these effects are evident in the solar and long wave heating rates measured during the SHEBA experiment (Figure 7). When solar flux is increased, clear sky conditions allow the pond surface to radiate more heat to space, for example, as indicated on day 15. In contrast, overcast conditions reduce solar radiation and can reverse the infrared flux direction as upward longwave flux is intercepted by clouds and reemitted as a downward flux, for example on day 23.

[44] In the next set of experiments, we use the melt pond model to examine the impact of variable solar radiation on pond evolution by contrasting conditions from mostly sunny and mostly overcast days. Surface forcing for these two conditions is estimated by selecting representative sunny and cloudy days from the SHEBA observations, and then repeating the daily cycle from these two samples for a 40 day simulation period. Here we select Day 190 as the ''sunny'' day conditions and Day 200 as the ''cloudy'' day conditions. Plots of the shortwave and longwave radiative fluxes for these two days are presented in Figure 12, and demonstrate the significant difference between the two forcing scenarios. Background ice bottom and surface melting rates are set to the same values as the control simulation with the more realistic, variable bottom albedo decreasing from 0.5 to 0.3 over the simulation period.

[45] Results from the two forcing scenarios are presented in Figure 13 along with the control simulation. Overall, the plots show a consistent behavior for the two scenarios that indicates the dominance of solar heating over insulation by overlying clouds. For example, pond fraction in the sunny case is almost 0.1 larger than the cloudy scenario with considerably deeper ponds averaging over 0.4 m versus 0.22 m for the cloudy case. Both pond and total albedo are slightly lower (about 0.04) for the sunny case in comparison with the cloudy scenario. Interestingly, at the end of the simulation, the control case is only slightly different from the cloudy scenario. The similarity between these two cases is generated by the much cooler conditions over the final 10 days of the control simulation, which are reflected in

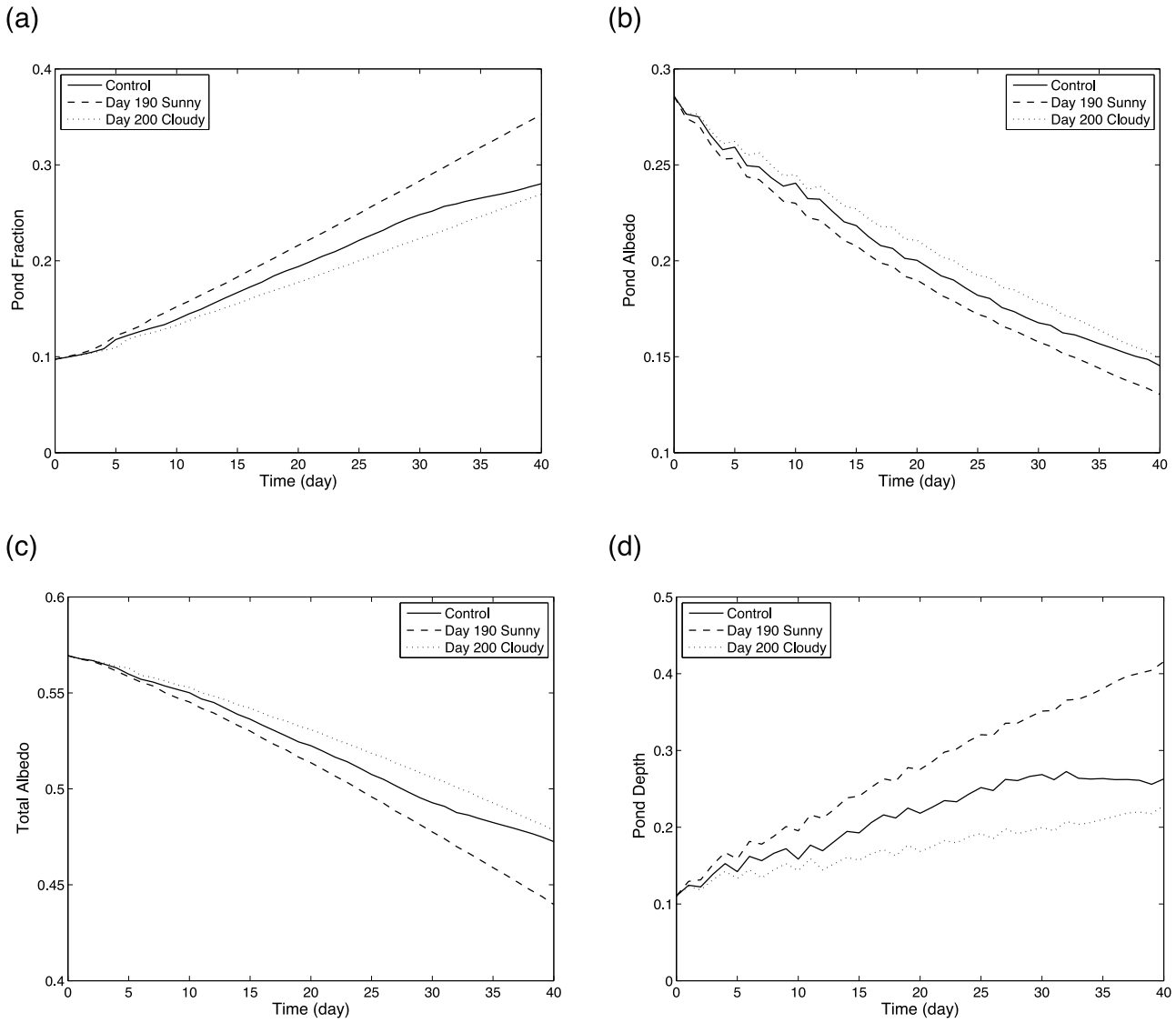

Figure 13. Plots for sunny (Day 190, dashed) and cloudy conditions (Day 200, dotted) along with the control case (solid) for (a) pond fraction, (b) pond albedo, (c) total albedo (assuming ice albedo of 0.6), and (d) pond depth (m). All cases have variable pond bottom albedo.

substantial heat loss from both sensible and latent heat. Thus, one conclusion we can make from these experiments is that overall, solar and longwave flux dominate the pond growth, but given the right conditions, surface fluxes of sensible and latent heat can dramatically change pond growth.

3.2.2. Surface Ice Melting Rates

[46] Pond depth is controlled both by melting in the pond and by changes in the overall ice pack that control the ice draft or local sea level. In our model, ponds are defined by depressions in the ice that extend below the local sea level as shown in Figure 1. In general the difference between the average ice thickness and ice draft decreases as the ice thins. However, if the pond bottom melts slower than the surface ice melting rate, then the pond depth can actually decrease with time as the surrounding surface ice melts.

[47] Simulating this behavior in the model was accomplished by conducting simulations using the control experiment ice conditions, but with variable surface ice melting rates between 0.5 and 2.0 cm d^{-1}. Results from these simulations are shown in Figure 14 and indicate that the surface ice melting rates can have a significant impact on the depth of modeled ponds. For example, with increased surface melting (2 cm d^{-1}), average pond depth increases only slightly over the 40 day experiment. In contrast, reduced surface melt (1 cm d^{-1}) enhances the pond depth growth, with average depth at the end of the experiment of $\sim$0.4 m. It is important to note that pond depth variations in these simulations are caused by the difference between melting rates of the surface ice versus the pond bottom. These differences define the rate at which pond depressions increase over time. They also alter the ice draft or water table, but this effect on pond depth is not as significant for the simulated ponds.

4. Conclusions

[48] A simplified sea ice model is used to simulate the evolution of melt ponds during the summer melt season.

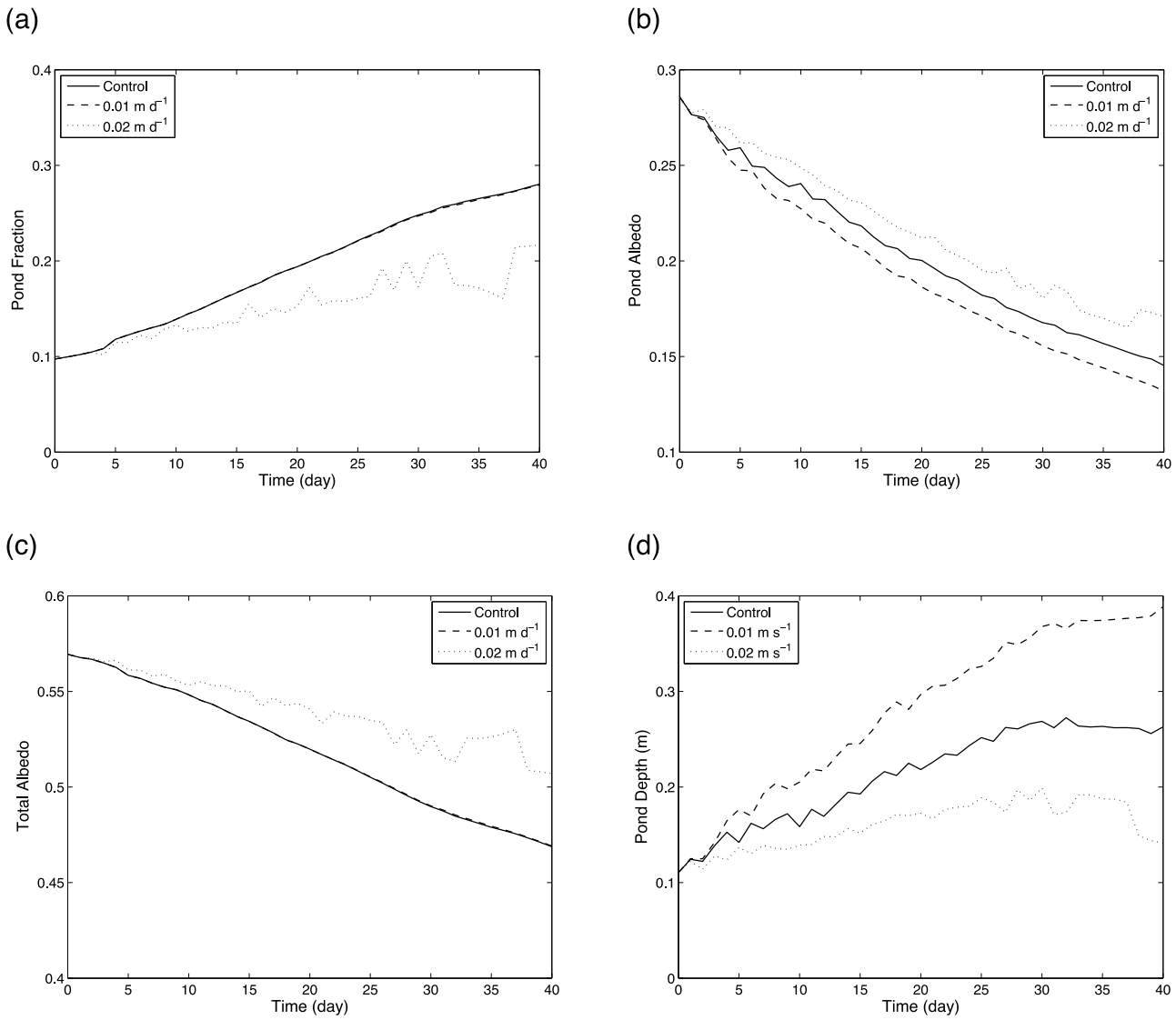

Figure 14. Average (a) pond fraction, (b) pond albedo, (c) total albedo (assuming ice albedo of 0.6), and (d) pond depth (m) with ice surface melting rates of 0.015 m s^{-1} (control), 0.01 m s^{-1}, and 0.02 m s^{-1}.

The model is based on the assumption that summer sea ice is porous and that ponds form in surface sea ice depressions. Pond depth in the model is set by the sea ice draft or local sea level, with meltwater flowing freely through the porous ice. Initialization of sea ice topography is estimated using aerial photographs of pond-covered ice during the 1998 SHEBA experiment. Pond depth is based on a radiative inverse calculation relating water depth to the pond albedo, which is estimated by scaling the image brightness intensity using an assumed pond-free ice surface albedo of 0.6.

[49] Using realistic forcing and model parameters, we show that the pond model yields reasonable estimates of key sea ice characteristics during SHEBA, such as the pond coverage, depth, and albedo. Experiments are conducted examining the role of solar heating, surface pond heat flux, and ice melting rates. Overall, we find that ponds increase linearly with time at a rate proportional to the combined incoming solar flux and heat loss from surface fluxes of latent, sensible and long wave radiation. Typically, heat gained from solar radiation is partially offset by heat lost via surface fluxes. Comparing representative cases for clear sky and cloudy sky conditions, we find that the insulative effect of clouds is not enough to offset the decrease in solar input. Consequently the pond coverage increases more rapidly under sunny conditions than in cloudy cases. This result is consistent with recent satellite observations suggesting that clear conditions have contributed to decreased sea ice [*Kay et al.*, 2008].

[50] Our model also predicts that pond depth and area are strongly related to surface ice melting rates. Surface ice melting rates that are larger than the pond bottom melting rates effectively reduce the differences in ice thickness that define ponds for porous ice leading to decreased pond depth. Realistically, however, it seems unlikely that the ice surface would melt faster than ice in contact with ponds given the higher absorption of solar radiation by darker ponds.

[51] Explicit parameterization of melt ponds in climate system models has only recently been attempted using relatively simple models. For example, the Los Alamos Sea Ice Model (CICE) represents ponds by calculating the total pond volume based on rates of ice and snow surface melting and rainfall [*Hunke and Lipscomb*, 2008]. The idea is that pond volume is defined by accumulating a fraction of the ice surface runoff of liquid water from melting and rainfall. This approach is consistent with conditions of thick, multiyear ice as discussed by *Fetterer and Untersteiner* [1998], where melt ponds are defined by water trapped on the ice surface in depressions. However, for first-year ice, or relatively thin multiyear ice, as observed during SHEBA and modeled here, this method may not be appropriate since pond depth and size are set by the freeboard and variations in the ice surface. Nevertheless, ice melt runoff could be considered a proxy for pond volume because of the correlation between ice melting and the surface heat budget. For our modeled ponds, time-integrated total surface heat flux ($Q_r + F_t$) increases much like the pond fraction as shown by Figure 15, supporting this approach. On a daily basis, however, the change in pond fractional area has a weak relationship with the total daily flux (Figure 16), suggesting that parameterizing melt ponds, at a minimum, requires some form of time-integrated heat for each ice-covered grid point. Ideally, pond fraction and depth should be explicitly considered as part of a more comprehensive melt pond parameterization.

[52] Many other questions remain concerning parameterization of melt ponds. For example, the frequent observation of pond free regions needs investigation. Do these regions have low thickness variability, with few depressions below the freeboard, or are they elevated so that water drains away? If ice surface topography determines the initial pond distribution, how do we model this effect? What ice thickness leads to an ice draft dependent pond field? How do ponds behave under more dynamic, windy conditions when fresh water is rapidly mixed with the underlying saline ocean? It is unlikely that physically based models can be developed that will accurately answer all of these questions. Ultimately, models will likely depend on statistical pond fractions that are constrained by observations and partitioned by ice age or thickness, much like current parameterizations. More robust ice measurements, both remote and on the surface, are needed to develop and improve these statistical descriptions.

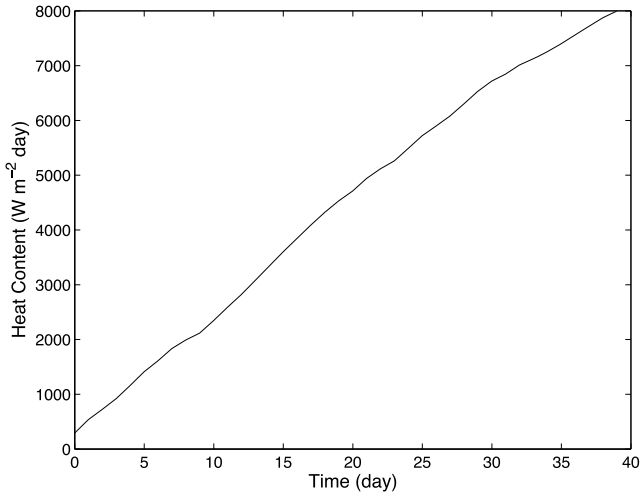

Figure 15. Time-integrated total heat flux (defined in text) over the 40 day experiment.

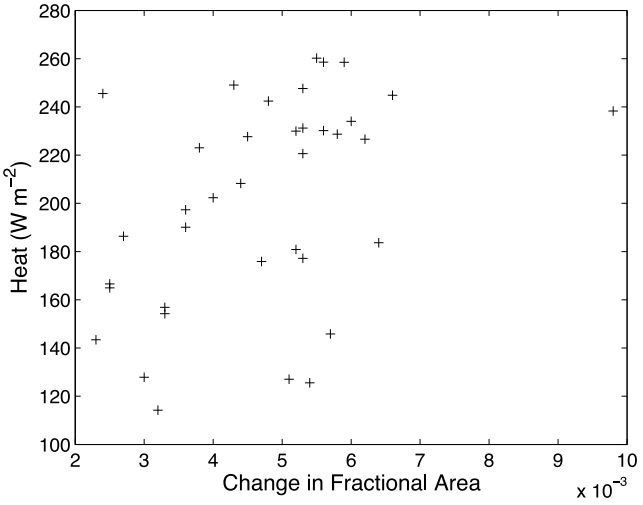

Figure 16. Daily average net heat flux plotted against the time rate of change of pond fractional area.

[53] As Arctic sea ice continues to change because of climatic conditions it is critical that differences between multiyear ice and first year ice be incorporated into climate models. Until recently, much of the Arctic ice cover was dominated by multiyear ice where melt ponds are often not governed by the ice draft as assumed here and observed during SHEBA. Unlike ponds on first-year ice or thin multiyear ice, ponds on thick multiyear ice may actually decrease in size as summer heating progresses [*Fetterer and Untersteiner*, 1998]. Modeling of thick, multiyear ice requires a more thorough treatment of the ice heating profile so that the depth of active ice melting can be separated from ice that is below the freezing point. Building a parameterization of both first year ice and more complicated multiyear ice will require a better understanding of the processes that control pond formation and evolution when the ice thermal structure is not uniform.

[54] **Acknowledgments.** We are pleased to acknowledge the supercomputer time provided by the National Center for Atmospheric Research, which is funded by the National Science Foundation. We thank Scott Pegau for assistance with the surface meteorological and flux data. We also thank the reviewers for their very useful comments. This research was funded by the National Science Foundation under grant ARC-0454867.

References

Barber, D. G., and J. Yackel (1999), The physical, radiative and microwave scattering characteristics of melt ponds on Arctic landfast sea ice, *Int. J. Remote Sens.*, *20*, 2069–2090, doi:10.1080/014311699212353.

Eicken, H., H. R. Krouse, D. Kadko, and D. K. Perovich (2002), Tracer studies of pathways and rates of meltwater transport through Arctic summer sea ice, *J. Geophys. Res.*, *107*(C10), 8046, doi:10.1029/2000JC000583.

Eicken, H., T. C. Grenfell, D. K. Perovich, J. A. Richter-Menge, and K. Frey (2004), Hydraulic controls of summer Arctic pack ice albedo, *J. Geophys. Res.*, *109*, C08007, doi:10.1029/2003JC001989.

Fetterer, F., and N. Untersteiner (1998), Observations of melt ponds on Arctic sea ice, *J. Geophys. Res.*, *103*, 24,821–24,835, doi:10.1029/98JC02034.

Hanesiak, J. M., D. G. Barber, R. A. De Abreu, and J. J. Yackel (2001), Local and regional albedo observations of arctic first-year sea ice during melt ponding, *J. Geophys. Res.*, *106*, 1005–1016, doi:10.1029/1999JC000068.

Hunke, E., and W. H. Lipscomb (2008), CICE: The Los Alamos sea ice model documentation and software user's manual version 4.0, *Tech. Rep. LA-CC-06–012*, Los Alamos Natl. Lab., Los Alamos, N. M.

Hvidegaard, S. M., and R. Forsberg (2002), Sea-ice thickness from airborne laser altimetry over the Arctic Ocean north of Greenland, *Geophys. Res. Lett.*, *29*(20), 1952, doi:10.1029/2001GL014474.

Kay, J. E., T. L'Ecuyer, A. Gettelman, G. Stephens, and C. O'Dell (2008), The contribution of cloud and radiation anomalies to the 2007 Arctic sea ice minimum, *Geophys. Res. Lett.*, *35*, L08503, doi:10.1029/2008GL033451.

Lüthje, M., D. L. Feltham, P. D. Taylor, and M. G. Worster (2006), Modeling the summertime evolution of sea-ice melt ponds, *J. Geophys. Res.*, *111*, C02001, doi:10.1029/2004JC002818.

McPhee, M. G. (1992), Turbulent heat flux in the upper ocean under sea ice, *J. Geophys. Res.*, *97*(C4), 5365–5379, doi:10.1029/92JC00239.

McPhee, M. G., G. A. Maykut, and J. H. Morison (1987), Dynamics and thermodynamics of the ice/upper ocean system in the marginal ice zone of the Greenland Sea, *J. Geophys. Res.*, *92*, 7017–7031, doi:10.1029/JC092iC07p07017.

Pegau, W. S. (2002), Inherent optical properties of the central Arctic surface waters, *J. Geophys. Res.*, *107*(C10), 8035, doi:10.1029/2000JC000382.

Perovich, D. K., T. C. Grenfell, B. Light, and P. V. Hobbs (2002a), Seasonal evolution of the albedo of multiyear Arctic sea ice, *J. Geophys. Res.*, *107*(C10), 8044, doi:10.1029/2000JC000438.

Perovich, D. K., W. B. Tucker III, and K. A. Ligett (2002b), Aerial observations of the evolution of ice surface conditions during summer, *J. Geophys. Res.*, *107*(C10), 8048, doi:10.1029/2000JC000449.

Perovich, D. K., T. C. Grenfell, J. A. Richter-Menge, B. Light, W. B. Tucker, and H. Eicken (2003), Thin and thinner: Ice mass balance measurements during SHEBA, *J. Geophys. Res.*, *108*(C3), 8050, doi:10.1029/2001JC001079.

Perovich, D. K., J. A. Richter-Menge, K. F. Jones, and B. Light (2008), Sunlight, water, and ice: Extreme Arctic sea ice melt during the summer of 2007, *Geophys. Res. Lett.*, *35*, L11501, doi:10.1029/2008GL034007.

Podgorny, I. A., and T. C. Grenfell (1996), Partioning of solar energy in melt ponds from measurements of pond albedo and depth, *J. Geophys. Res.*, *101*, 22,737–22,748, doi:10.1029/96JC02123.

Serreze, M. C., M. M. Holland, and J. Stroeve (2007), Perspectives on the Arctic's shrinking sea-ice cover, *Science*, *315*, 1533–1536, doi:10.1126/science.1139426.

Skyllingstad, E. D., and C. A. Paulson (2007), A numerical simulations of melt ponds, *J. Geophys. Res.*, *112*, C08015, doi:10.1029/2006JC003729.

Sneed, W. A., and G. S. Hamilton (2007), Evolution of melt pond volume on the surface of the Greenland Ice Sheet, *Geophys. Res. Lett.*, *34*, L03501, doi:10.1029/2006GL028697.

Stroeve, J., M. M. Holland, W. Meier, T. Scambos, and M. Serrezem (2007), Arctic sea ice decline: Faster than forecast, *Geophys. Res. Lett.*, *34*, L09501, doi:10.1029/2007GL029703.

Stull, R. B. (1988), *An Introduction to Boundary Layer Meteorology*, 666 pp., Kluwer Acad., Dordrecht, Netherlands.

Taylor, P. D., and D. L. Feltham (2004), A model of melt pond evolution on sea ice, *J. Geophys. Res.*, *109*, C12007, doi:10.1029/2004JC002361.

Yackel, J. J., D. G. Barber, and J. M. Hanesiak (2000), Melt ponds on sea ice in the Canadian Archipelago: 1. Variability in morphological and radiative properties, *J. Geophys. Res.*, *105*, 22,049–22,060.

C. A. Paulson and E. D. Skyllingstad, College of Oceanic and Atmospheric Sciences, Oregon State University, Corvallis, OR 97331, USA. (skylling@coas.oregonstate.edu)

D. K. Perovich, Cold Regions Research and Engineering Laboratory, U.S. Army Engineer Research and Development Center, 72 Lyme Rd., Hanover, NH 03755, USA.